

Unsupervised Deep Homography: A Fast and Robust Homography Estimation Model

Ty Nguyen, Steven W. Chen, Shreyas S. Shivakumar, Camillo J. Taylor, Vijay Kumar

Abstract—This paper develops an unsupervised learning algorithm that trains a Deep Convolutional Neural Network to estimate planar homographies. The traditional feature-based approaches to estimating can fail when good features cannot be identified, and can be slow during the feature identification and matching process. We demonstrate that our unsupervised algorithm outperforms these traditional approaches in accuracy, speed, and robustness to noise on both synthetic images and real-world images captured from a UAV. In addition, we demonstrate that our unsupervised method has superior performance compared to the corresponding supervised method of training the network architecture using ground truth homography labels. Our approach is a general motion estimation framework that can be extended beyond estimating planar homographies to more general motions such as optical flow.

I. INTRODUCTION

A homography is a mapping between two images of a planar surface from different perspectives. They play an essential role in robotics and computer vision applications such as image mosaicing [1], monocular SLAM [2], 3D camera pose reconstruction [3] and virtual touring [4], [5]. For example, homographies are applicable in scenes viewed at a far distance by an arbitrary moving camera [6], which are the situations encountered in UAV and satellite photography.

The two traditional approaches for homography estimation are direct methods and feature-based methods [7]. Direct methods, such as the seminal Lucas-Kanade algorithm [8], use pixel-to-pixel matching by shifting or warping the images relative to each other and comparing the pixel intensity values using an error metric such as the sum of squared differences (SSD). They initialize a guess for the homography parameters and use a search or optimization technique such as gradient descent to minimize the error function [9]. The problem with direct methods is that they have limited range of convergence, and are slow due to the search process.

The second, more common, approach are feature-based methods. These methods first extract keypoints in each image using local invariant features (e.g. Scale Invariant Feature Transform (SIFT) [10]). They then establish a correspondence between the two sets of keypoints using feature matching, and use RANSAC [11] to find the best homography estimate. While these methods have better performance than direct methods, they can be inaccurate when they fail to detect sufficient keypoints, or produce incorrect keypoint correspondences due to illumination and large viewpoint differences between the images [12]. In addition, while these

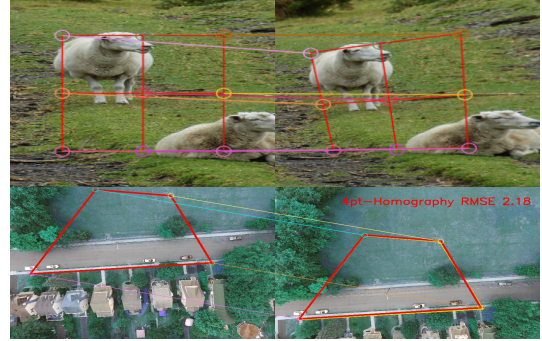


Fig. 1: Above: Synthetic data; Below: Real data; Homography estimation with unsupervised neural network.

methods are significantly faster than direct methods, the computation of the features can still be slow, leading to the development of other feature types such as Oriented FAST and Rotated BRIEF (ORB) [13] which are more computationally efficient than SIFT, but have worse performance.

Inspired by the success of data-driven Deep Convolutional Neural Networks (CNN) in computer vision, there has been an emergence of CNN approaches to estimating optical flow [14], [15], [16], dense matching [17], [18], depth estimation [19], and homography estimation [20]. Most of these works, including the most relevant work on homography estimation, treat the estimation problem as a supervised learning task. These supervised approaches use ground truth labels, and as a result are limited to synthetic datasets where the ground truth can be generated for free, or require costly labeling of real-world data sets.

Our work develops an unsupervised, end-to-end, deep learning algorithm to estimate homographies. It improves upon these prior traditional and supervised learning methods by minimizing a pixel-wise intensity error metric that does not need ground truth data. Unlike the hand-crafted feature-based approaches, or the supervised approach that needs costly labels, our model is adaptive and can easily learn good features specific to different data sets. Furthermore, our framework has fast inference times since it is highly parallel. These adaptive and speed properties make our unsupervised networks especially suitable for real world robotic tasks, such as stitching UAV images.

We demonstrate that our homography estimation algorithm outperforms both traditional feature-based methods and supervised deep learning methods in accuracy, inference speed, and robustness to noise on synthetic and real-world UAV data sets. Fig. 1 illustrates qualitative results on these data sets.

The authors are with GRASP Lab, University of Pennsylvania, Philadelphia, PA 19104, USA, {tynguyen, chenste, sshreyas, cjtaylor, kumar}@seas.upenn.edu.

Our unsupervised algorithm is a hybrid approach that combines the strengths of deep learning with the strengths of both traditional direct methods and feature based methods. It is similar to feature-based methods because it also relies on features to compute the homography estimates, but it differs in that it learns the features rather than defining them. It is also similar to the direct methods because the error signal used to drive the network training is a pixel-wise error. However, rather than performing an online optimization process, it transfers the computation offline and "caches" the results through these learned features. Similar unsupervised deep learning approaches have been successful in computer vision tasks such as monocular depth and camera motion estimation [21], indicating that our framework can be scaled to tackle general nonlinear motions such as those encountered in optical flow.

II. PROBLEM FORMULATION

We assume that images are obtained by a perspective pin-hole camera and present points by homogeneous coordinates, so that a point $(u, v)^T$ is represented as $(u, v, 1)^T$ and a point $(x, y, z)^T$ is equivalent to the point $(x/z, y/z, 1)^T$. Suppose that $\mathbf{x} = (u, v, 1)^T$ and $\mathbf{x}' = (u', v', 1)^T$ are two points. A planar projective transformation or homography that maps $\mathbf{x} \leftrightarrow \mathbf{x}'$ is a linear transformation represented by a non-singular 3×3 matrix \mathbf{H} such that:

$$\begin{bmatrix} u' \\ v' \\ 1 \end{bmatrix} = \begin{bmatrix} h_{11} & h_{12} & h_{13} \\ h_{21} & h_{22} & h_{23} \\ h_{31} & h_{32} & h_{33} \end{bmatrix} \begin{bmatrix} u \\ v \\ 1 \end{bmatrix} \quad \text{Or} \quad \mathbf{x}' = \mathbf{H}\mathbf{x} \quad (1)$$

Since \mathbf{H} can be multiplied by an arbitrary non-zero scale factor without altering the projective transformation, only the ratio of the matrix elements is significant, leaving \mathbf{H} eight independent ratios corresponding to eight degrees of freedom. This mapping equation can also be represented by two equations:

$$u' = \frac{h_{11}u + h_{12}v + h_{13}}{h_{31}u + h_{32}v + h_{33}}; v' = \frac{h_{21}u + h_{22}v + h_{23}}{h_{31}u + h_{32}v + h_{33}} \quad (2)$$

The problem of finding the homography induced by two images I^A and I^B is to find a homography \mathbf{H}^{AB} such that Eqn. (1) holds for all points in the overlapping of the two images.

III. CURRENT STATE OF THE ART METHODS

This section details the feature-based method and the supervised deep CNN method to estimating homographies which are the comparative benchmarks for our unsupervised algorithm. Since feature-based methods are more common and known to be more robust than direct methods, we will not compare our approach to a direct method.

A. Feature-based Methods

Feature-based methods first detect and describe keypoints using feature detector and descriptors. A generic feature-based approach includes steps depicted in Fig. 2(b). As previously mentioned, two common feature detectors and descriptors are SIFT and ORB. SIFT is scale-invariant and

is the benchmark for feature-based methods, while ORB is a faster alternative.

After independently finding keypoints in each image, a feature matching algorithm is used to find a minimum of 4 keypoint pairs $\mathbf{x} \leftrightarrow \mathbf{x}'$. Some popular feature matching methods are Fast Library for Approximate Nearest Neighbors (FLANN) based search [22] or brute-force search. Each keypoint pair provides 2 degrees of freedom $(\Delta u, \Delta v)$, giving the necessary 8 degrees of freedom to compute the homography using either the direct linear transform (DLT) or singular value decomposition (SVD) [23].

The difficulty with using only 4 points is that a correspondence outlier can yield inaccurate homography estimates. To provide robustness, RANSAC is often used after finding a set of N correspondences from the feature matching step to reject outliers and produce the final homography estimate.

B. Deep Learning Methods

The deep learning approach most similar to our work is the Deep Image Homography Estimation [20]. In this work, DeTone et al. use supervised learning to train a deep neural network on a synthetic data set. They use the 4-point homography parameterization \mathbf{H}_{4pt} [24] rather than the conventional 3×3 parameterization \mathbf{H} . Suppose that $\mathbf{u}_k^A = (u_k^A, v_k^A, 1)^T$ and $\mathbf{u}_k^B = (u_k^B, v_k^B, 1)^T$ for $k = 1, 2, 3, 4$ are 4 fixed points in image I^A and I^B respectively, such that $\mathbf{u}_2^k = \mathbf{H}\mathbf{u}_1^k$. Let $\Delta u_k = u_k^B - u_k^A$, $\Delta v_k = v_k^B - v_k^A$. Then \mathbf{H}_{4pt} is the 4×2 matrix of points $(\Delta u_k, \Delta v_k)$. Both parameterizations are equivalent since there is a one-to-one correspondence between them.

In a deep learning framework though, this parameterization is more suitable than the 3×3 parameterization \mathbf{H} because \mathbf{H} mixes the rotation, translation, scale, and shear components of the homography transformation. The rotation and shear components tend to have a much smaller magnitude than the translation component, and as a result although an error in their values can greatly impact \mathbf{H} , it will have a small effect on the L^2 loss function of the elements of \mathbf{H} , which is detrimental for training the neural network. In addition, the high variance in the magnitude of the elements of the 3×3 homography matrix makes it difficult to enforce \mathbf{H} to be non-singular. The 4-point parameterization does not suffer from these problems.

The network architecture is based on VGGNet [25], and is depicted in Fig. 2(a). The network input is a batch of image patch pairs. The patch pairs are generated by taking a full-sized image, cropping a square patch P^A at a random position p , perturbing the four corners of by a random value within $[-\rho, \rho]$ to generate a homography \mathbf{H}^{AB} , applying $(\mathbf{H}^{AB})^{-1}$ to the full-sized image, and then cropping a square patch P^B of the same size and at the same location as the patch P^A from the warped image. These image patches are used to avoid strange border effects near the edges during the synthetic data generation process, and to standardize the network input size. The applied homography \mathbf{H}^{AB} is saved in the 4 point parameterization format, \mathbf{H}_{4pt}^* . The network outputs a 4 point parameterization estimate $\hat{\mathbf{H}}_{4pt}$.

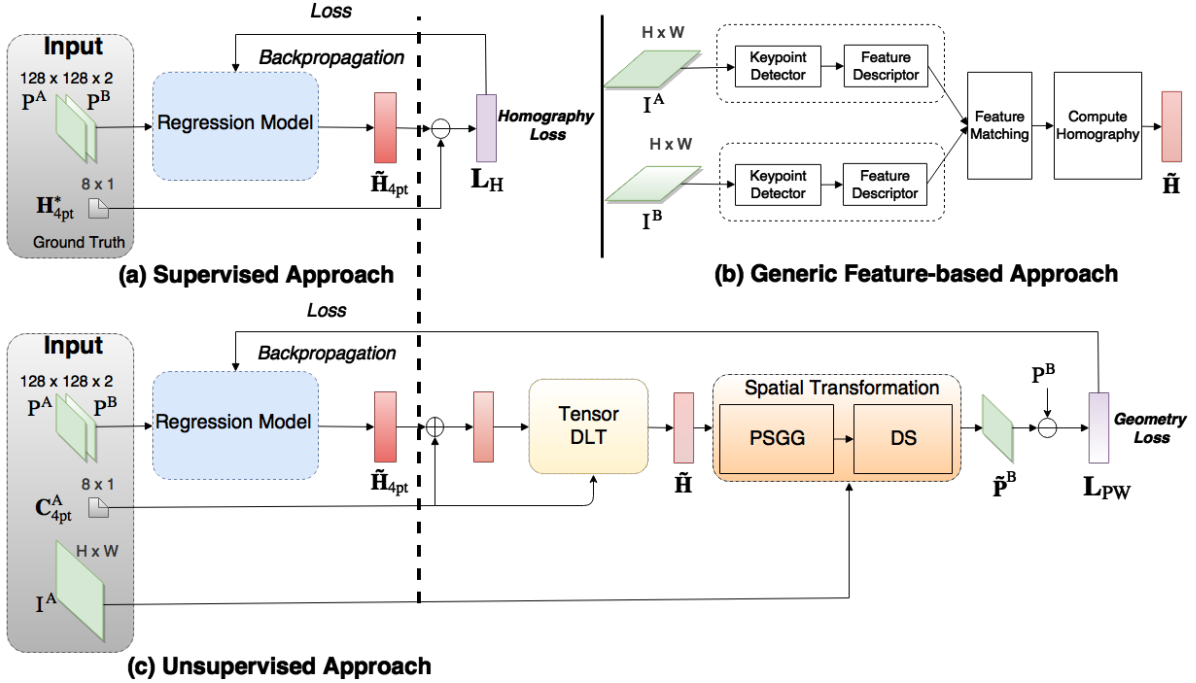


Fig. 2: Overview of homography estimation methods; (a) Benchmark supervised deep learning approach; (b) Feature-based methods; and (c) Our unsupervised method. DLT: direct linear transform; PSGG: parameterized sampling grid generator; DS: differentiable sampling.

The error signal used for gradient backpropagation is the Euclidean L^2 norm, denoted as L_H , of the estimated 4-point homography $\tilde{\mathbf{H}}_{4pt}$ versus the ground truth \mathbf{H}_{4pt}^* :

$$L_H = \frac{1}{2} \|\tilde{\mathbf{H}}_{4pt} - \mathbf{H}_{4pt}^*\|_2^2 \quad (3)$$

IV. UNSUPERVISED DEEP HOMOGRAPHY MODEL

While the supervised deep learning method has promising results, it is limited in real world applications since it requires ground truth labels. Drawing inspiration from traditional direct methods for homography estimation, we can define an analogous loss function. Given an image pair $I^A(\mathbf{x})$ and $I^B(\mathbf{x})$ with discrete pixel locations represented by homogeneous coordinates $\{\mathbf{x}_i = (x_i, y_i, 1)^T\}$, we want our network to output $\tilde{\mathbf{H}}_{4pt}$ that minimizes the pixel-wise root mean square error (RMSE)

$$L_{PW} = \frac{1}{2|\mathbf{x}_i|} \sqrt{\sum_{\mathbf{x}_i} [I^A(\mathcal{H}(\mathbf{x}_i)) - I^B(\mathbf{x}_i)]^2} \quad (4)$$

where $\tilde{\mathbf{H}}_{4pt}$ defines the homography transformation $\mathcal{H}(\mathbf{x}_i)$. This loss function is unsupervised since there is no ground truth label. Similar to the supervised case, the 4-point parameterization is more suitable than the 3×3 parameterization, so we will use 4-point parameterization in our model.

In order to compare our unsupervised deep learning algorithm with the supervised algorithm, we use the same VGGNet architecture to output the $\tilde{\mathbf{H}}_{4pt}$. Fig. 2(c) depicts our unsupervised learning model. The regression module represents the VGGNet architecture and is shared by both the supervised and unsupervised methods. Although we do not

investigate other possible architectures, different regression models such as SqueezeNet [26] may yield better performance due to advantages in size and computation requirements. The second half of Fig. 2(c) represents the main contribution of this work, which consists of the differentiable layers that allow the network to be successfully trained with the loss function (4).

Using the pixel-wise RMSE loss function yields additional training challenges. First, every operation, including the warping operation $\mathcal{H}(\mathbf{x}_i)$, must remain differentiable to allow the network to be trained via backpropagation. Second, since the error signal depends on differences in image intensity values rather than the differences in the homography parameters, training the deep network is not necessarily as easy or stable. Another implication of using a pixel-wise intensity based RMSE loss function is the implied assumption that lighting and contrast between the input images remains consistent.

A. Model Inputs

The input to our model consists of three parts. The first part is a 2-channel image of size $128 \times 128 \times 2$ which is the stack of P^A and P^B - two patches cropped from the two images I^A and I^B . The second part is the four corners in I^A , denoted as C_{4pt}^A . Image I^A is also part of the input as it is necessary for warping.

B. Tensor Direct Linear Transform

We develop a Tensor Direct Linear Transform (Tensor DLT) layer to compute a differentiable mapping from the 4-point parameterization $\tilde{\mathbf{H}}_{4pt}$ to $\tilde{\mathbf{H}}$, the 3×3 parameterization

of homography. This layer essentially applies the DLT algorithm [9] to tensors, while remaining differentiable to allow backpropagation during training. As shown in Fig. 2(c), the input to this layer are the corresponding corners in the image pairs \mathbf{C}_{4pt}^A and $\tilde{\mathbf{C}}_{4pt}^B$, and the output is the estimate of the 3×3 homography parameterization $\tilde{\mathbf{H}}$.

The DLT algorithm is used to solve for the homography matrix \mathbf{H} given a set of four point correspondences [27]. Let \mathbf{H} be the homography induced by a set of four 2D to 2D correspondences, $\mathbf{x}_i \leftrightarrow \mathbf{x}'_i$. According to the definition of a homography given in Eqn. (1), $\mathbf{x}'_i \sim \mathbf{H}\mathbf{x}_i$. This relation can also be expressed as $\mathbf{x}'_i \times \mathbf{H}\mathbf{x}_i = 0$.

Let \mathbf{h}^{jT} be the j -th row of \mathbf{H} , then:

$$\mathbf{H}\mathbf{x}_i = \begin{bmatrix} \mathbf{h}^{1T} \mathbf{x}_i \\ \mathbf{h}^{2T} \mathbf{x}_i \\ \mathbf{h}^{3T} \mathbf{x}_i \end{bmatrix} = \begin{bmatrix} \mathbf{x}_i^T \mathbf{h}^1 \\ \mathbf{x}_i^T \mathbf{h}^2 \\ \mathbf{x}_i^T \mathbf{h}^3 \end{bmatrix} \quad (5)$$

where \mathbf{h}^j is the column vector representation of \mathbf{h}^{jT} .

Let $\mathbf{x}'_i = (u'_i, v'_i, 1)^T$, then:

$$\mathbf{x}'_i \times \mathbf{H}\mathbf{x}_i = \begin{bmatrix} v'_i \mathbf{x}_i^T \mathbf{h}^3 - \mathbf{x}_i^T \mathbf{h}^2 \\ \mathbf{x}_i^T \mathbf{h}^1 - u'_i \mathbf{x}_i^T \mathbf{h}^3 \\ u'_i \mathbf{x}_i^T \mathbf{h}^2 - v'_i \mathbf{x}_i^T \mathbf{h}^1 \end{bmatrix} = 0 \quad (6)$$

This equation can be rewritten as:

$$\begin{bmatrix} 0_{3 \times 1}^T & -\mathbf{x}_i^T & v'_i \mathbf{x}_i^T \\ \mathbf{x}_i^T & 0_{3 \times 1}^T & -u'_i \mathbf{x}_i^T \\ -v'_i \mathbf{x}_i^T & u'_i \mathbf{x}_i^T & 0_{3 \times 1}^T \end{bmatrix} \begin{bmatrix} \mathbf{h}^1 \\ \mathbf{h}^2 \\ \mathbf{h}^3 \end{bmatrix} = 0. \quad (7)$$

which has the form $\mathbf{A}_i^{(3)} \mathbf{h} = \mathbf{0}$ for each $i = 1, 2, 3, 4$ correspondence pair, where $\mathbf{A}_i^{(3)}$ is a 3×9 matrix, and \mathbf{h} is a vector with 9 elements consisting of the entries of \mathbf{H} . Since the last row in $\mathbf{A}_i^{(3)}$ is dependent on the other rows, we are left with two linear equations $\mathbf{A}_i \mathbf{h} = \mathbf{0}$ where \mathbf{A}_i is the first 2 rows of $\mathbf{A}_i^{(3)}$.

Given a set of 4 correspondences, we can create a system of equations to solve for \mathbf{h} and thus \mathbf{H} . For each i , we can stack \mathbf{A}_i to form $\mathbf{A}\mathbf{h} = \mathbf{0}$. Solving for \mathbf{h} results in finding a vector in the null space of \mathbf{A} . One popular approach is singular value decomposition (SVD) [28], which is a differentiable operation. However, taking the gradients in SVD has high time complexity and has practical implementation issues [29]. An alternative solution is to make the assumption that the last element of $\mathbf{h}^3 = \mathbf{H}_{33}$ equals 1 [30].

With this assumption and the fact that $\mathbf{x}_i = (u_i, v_i, 1)$, we can rewrite Eqn. (7) in the form $\hat{\mathbf{A}}_i \hat{\mathbf{h}} = \hat{\mathbf{b}}_i$ for each $i = 1, 2, 3, 4$ correspondence points where $\hat{\mathbf{A}}_i$ is the 2×8 matrix representing the first 8 columns of \mathbf{A}_i ,

$$\hat{\mathbf{A}}_i = \begin{bmatrix} 0 & 0 & 0 & -u_i & -v_i & -1 & v'_i u_i & v'_i v_i \\ u_i & v_i & 1 & 0 & 0 & 0 & -u'_i u_i & -u'_i v_i \end{bmatrix},$$

$\hat{\mathbf{b}}_i$ is a vector with 2 elements representing the last column of \mathbf{A}_i subtracted from both sides of the equation,

$$\hat{\mathbf{b}}_i = [-v'_i, u'_i]^T,$$

and $\hat{\mathbf{h}}$ is a vector consisting of the first 8 elements of \mathbf{h} (with \mathbf{H}_{33} omitted).

By stacking these equations, we get:

$$\hat{\mathbf{A}} \hat{\mathbf{h}} = \hat{\mathbf{b}}, \quad (8)$$

Eqn. (8) has a desirable form because $\hat{\mathbf{h}}$, and thus \mathbf{H} , can be solved for using $\hat{\mathbf{A}}^+$, the pseudo-inverse of $\hat{\mathbf{A}}$. This operation is simple and differentiable with respect to the coordinates of \mathbf{x}_i and \mathbf{x}'_i . In addition, the gradients are easier to calculate than for SVD.

This approach may still fail if the correspondence points are collinear: if three of the correspondence points are on the same line, then solving for \mathbf{H} is undetermined. We alleviate this problem by first making the initial guess of \mathbf{H}_{4pt} to be zero, implying that $\tilde{\mathbf{C}}_{4pt}^B \sim \mathbf{C}_{4pt}^A$. We then set a small learning rate such that after each training iteration, $\tilde{\mathbf{C}}_{4pt}^B$ does not move too far away from \mathbf{C}_{4pt}^A .

C. Spatial Transformation Layer

The next layer applies the 3×3 homography estimate $\tilde{\mathbf{H}}$ output by the Tensor DLT to the pixel coordinates \mathbf{x}_i of image I^A in order to get warped coordinates $\mathcal{H}(\mathbf{x}_i)$. These warped coordinates are necessary in computing the pixel-wise RMSE loss function in Eqn. (4) that will train our neural network. In addition to warping the coordinates, this layer must also be differentiable so that the error gradients can flow through via backpropagation. We thus extend the Spatial Transformer Layer introduced in [31] by applying it to homography transformations.

This layer performs an inverse warping in order to avoid holes in the warped image. This process consists of 3 steps: (1) Normalized inverse computation $\tilde{\mathbf{H}}_{inv}$ of the homography estimate; (2) Parameterized Sampling Grid Generator (PSGG); and (3) Differentiable Sampling (DS).

The first step, computing a normalized inverse, involves normalizing the height and width coordinates of images I^A and I^B into a range such that $-1 \leq u_i, v_i \leq 1$ and $-1 \leq u'_i, v'_i \leq 1$. Thus given a 3×3 homography estimate $\tilde{\mathbf{H}}$, the inverse $\tilde{\mathbf{H}}_{inv}$ used for warping is computed as follows:

$$\tilde{\mathbf{H}}_{inv} = M^{-1} \tilde{\mathbf{H}}^{-1} M$$

$$\text{where } M = \begin{bmatrix} W'/2 & 0 & W'/2 \\ 0 & H'/2 & H'/2 \\ 0 & 0 & 1 \end{bmatrix}$$

with W' and H' are the width and height of the I_B .

The second step (PSGG) creates a grid $G = \{G_i\}$ of the same size as the second image I^B . Each grid element $G_i = (u'_i, v'_i)$ corresponds to pixels of the second image I^B . Applying the inverse homography $\tilde{\mathbf{H}}_{inv}$ to these grid coordinates provides a grid of pixels in the first image I^A .

$$\begin{bmatrix} u_i \\ v_i \\ 1 \end{bmatrix} = \mathcal{H}_{inv}(G_i) = \tilde{\mathbf{H}}_{inv} \begin{bmatrix} u'_i \\ v'_i \\ 1 \end{bmatrix} \quad (9)$$

Based on the sampling points $\mathcal{H}_{inv}(G_i)$ computed from PSGG, the last step (DS) produces a sampled warped image V of size $H' \times W'$ with C channels, where $V(\mathbf{x}_i) = I^A(\mathcal{H}(\mathbf{x}_i))$.

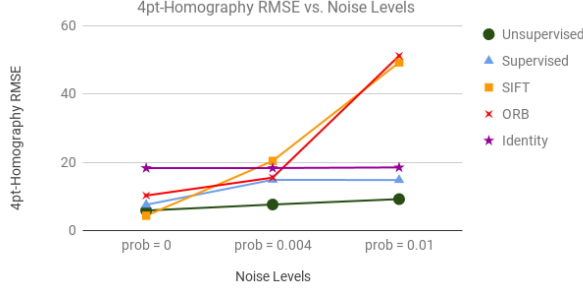


Fig. 3: 4pt-Homography RMSE on synthetic dataset (lower is better). Unsupervised has best performance across noise levels.

The sampling kernel $k(\cdot)$ is applied to the grid $\mathcal{H}_{inv}(G_i)$ and the resulting image V is defined as

$$V_i^c = \sum_n^H \sum_m^W I_{nm}^c k(u_i - m; \Phi_u) k(v_i - n; \Phi_v), \quad \forall i \in [1 \dots H'W'] \quad , \forall c \in [1 \dots C] \quad (10)$$

where H, W are the height and width of the input image I^A , Φ_u and Φ_v are the parameters of $k(\cdot)$ defining the image interpolation. I_{nm}^c is the value at location (n, m) in channel c of the input image, and V_i^c is the value of the output pixel at location (u_i, v_i) in channel c . Here, we use bilinear interpolation such that the Eqn. (10) becomes

$$V_i^c = \sum_n^H \sum_m^W I_{nm}^c \max(0, 1 - |u_i - m|) \max(0, 1 - |v_i - n|) \quad (11)$$

To allow backpropagation of the loss function, gradients with respect to I and G for bilinear interpolation are defined as

$$\frac{\partial V_i^c}{\partial I_{nm}^c} = \sum_n^H \sum_m^W \max(0, 1 - |u_i - m|) \max(0, 1 - |v_i - n|) \quad (12)$$

$$\frac{\partial V_i^c}{\partial u_i} = \sum_n^H \sum_m^W I_{nm}^c \max(0, 1 - |v_i - n|) \begin{cases} 0 & \text{if } |m - u_i| \geq 1 \\ 1 & \text{if } m \geq u_i \\ -1 & \text{if } m < u_i \end{cases} \quad (13)$$

$$\frac{\partial V_i^c}{\partial v_i} = \sum_n^H \sum_m^W I_{nm}^c \max(0, 1 - |u_i - m|) \begin{cases} 0 & \text{if } |n - v_i| \geq 1 \\ 1 & \text{if } n \geq v_i \\ -1 & \text{if } n < v_i \end{cases} \quad (14)$$

This allows backpropagation of the loss gradients because $\frac{\partial u_i}{\partial h_{jk}}$ and $\frac{\partial v_i}{\partial h_{jk}}$ can be easily derived from Eqn. 2.

V. EVALUATION RESULTS

We demonstrate the effectiveness of our unsupervised algorithm by comparing its accuracy, inference speed, and robustness to noise relative to SIFT, ORB, and the supervised deep learning method. We evaluate these methods on a synthetic data set similar to the one used in [20] and on a real-world UAV data set.

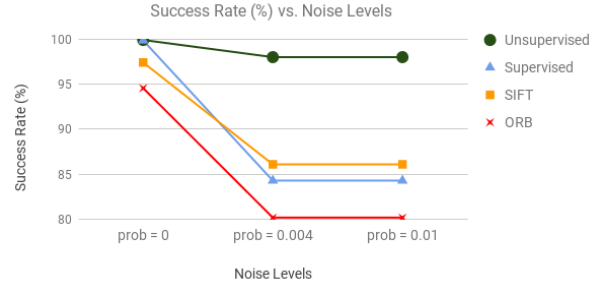


Fig. 4: Success rate on synthetic dataset (higher is better). Unsupervised has highest success rates. Success measures consistency and is defined relative to identity homography.

A. Implementation Details

Both the supervised and unsupervised approaches use the VGGNet architecture to generate homography estimates $\hat{\mathbf{H}}_{4pt}$. The deep learning approaches are implemented in Tensorflow [32], both trained using stochastic gradient descent with a batch size of 64, and an Adam Optimizer [33] with an initial learning rate 0.001, $\beta_1 = 0.9$, $\beta_2 = 0.999$ and $\epsilon = 10^{-8}$.

The feature-based approaches are Python OpenCV implementations of SIFT RANSAC and ORB RANSAC, which we will refer to as SIFT and ORB. After detecting features, we use a brute-force matcher using the Euclidean distance (SIFT) and Hamming distance (ORB) to match and choose the 25 best correspondences. These pairs are then used to calculate the homography using RANSAC with a threshold of 5 pixels.

B. Synthetic Data Results

Our synthetic data generation process uses the MS-COCO training dataset to generate 100,000 training samples, and the MS-COCO test dataset to generate 5,000 test samples. First, we randomly select an image I^A in the MS-COCO dataset and resize it to 240×320 . We then crop a square 128×128 patch p at a random position to get the first patch P^A and 4 corner points called C_{4pt}^A . These four points are perturbed within a range $[-32, 32]$ to form another four points C_{4pt}^B . We compute a homography \mathbf{H}^{AB} induced by correspondences C_{4pt}^A and apply its inverse $(\mathbf{H}^{AB})^{-1}$ to the large image to create the second image I^B . We crop I^B at the same position p to obtain the second patch P^B . Each data sample now is a set consisting of P^A, P^B, C_{4pt}^A and the 4pt-Homography ground truth $\mathbf{H}_{4pt}^* = C_{4pt}^B - C_{4pt}^A$. We create 4 such samples per large image for the training set and 1 sample per large image for the test set.

We test robustness to noise by injecting salt-and-pepper noise into the images I^A, I^B . We create three test sets by randomly changing the pixel intensity to 0 and 255 with a probability equal to ϵ and $1 - \epsilon$ respectively, where $\epsilon = 0, 0.004, 0.01$. Each channel of each pixel is injected noise independently. This noise mimics errors that can occur during analog to digital conversion or data transfer.

We use two evaluation metrics on these test sets. The first metric is the 4pt-Homography RMSE provided in Eqn. (3),

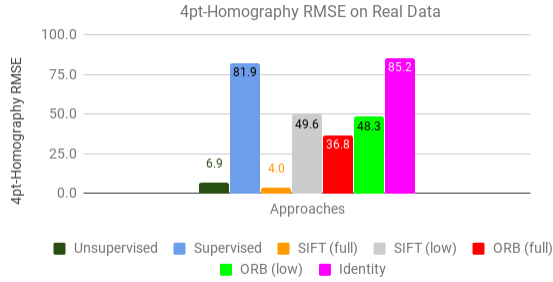


Fig. 5: 4pt-homography RMSE on real images (lower is better). Unsupervised and SIFT (full) have comparable performance.

and evaluates the $\tilde{\mathbf{H}}_{4pt}$ output with the ground truth \mathbf{H}_{4pt}^* . The second metric is a success rate where success is defined as achieving a lower 4pt-Homography RMSE relative to the identity homography. In practical applications, such as image mosaicing, a single failed homography estimation can throw off the entire sequential procedure. As a result, an ideal homography estimation approach must consistently provide good estimates, not just on the average.

We train the deep networks from scratch for 90,000 iterations over ~ 27 hours. This long training procedure only needs to be performed once, as the resulting model can be used as an initial pre-trained model for other data sets. The homography estimate is a forward pass through the networks. For SIFT and ORB, rather than using a small patch, we input the full 240×320 size images to estimate the homography $\tilde{\mathbf{H}}_{4pt}$, which allows them to compute better features.

We evaluate every approach on each test set 30 times and report the average of 4pt-Homography RMSE and success rate. Results are shown in Fig. 3 and Fig. 4. At all noise levels and in both metrics, our unsupervised method outperforms the supervised method even though the supervised method is directly minimizing the 4pt-Homography RMSE evaluation metric, while our unsupervised method is minimizing the pixel-wise RMSE error. The regression model is shared by both methods, so the performance gains are due to the different loss function.

In terms of the 4pt-Homography RMSE, SIFT slightly outperforms our unsupervised method with no noise, however ORB has lower accuracy. Our method has much better performance than both feature-based methods as noise is injected, indicating that our method is more robust to salt-and-pepper noise.

In terms of the success rate, our method outperforms the feature-based methods with 95% success even at the highest noise level compared to 78% for SIFT and ORB. These results indicate that feature-based methods are brittle in that they perform well if they identify enough feature points, but will fail in situations where not enough good feature correspondences are detected.

In addition to having better performance, our method does not need hand-labeled data. This benefit has large practical importance, which will be demonstrated in the real

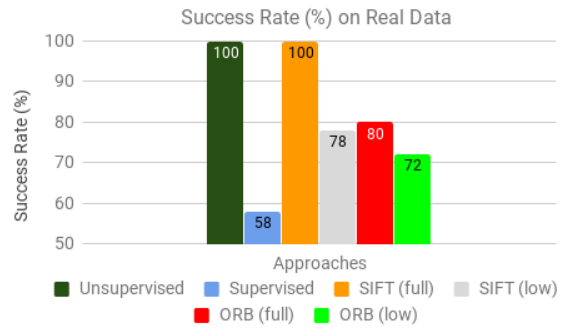


Fig. 6: Success rate on real images (higher is better). Unsupervised and SIFT (full) have 100% success rate.

data set. The requirement of ground-truth labels limits the applicability of the supervised method to specific scenarios, i.e. synthetic data generation. This training regime may not be similar to those encountered in real-world scenarios, and as a result, there will be a large gap between the "train" and "test" distributions, which will negatively impact accuracy. On the contrary, our unsupervised approach can be applied to any data set, and as result can be trained on a data set that is as similar to the testing environment as possible. An example of this would be the quickly collect a dataset of images at a deployment site and finetune the network using our unsupervised method.

C. Real-Data Results

Our real data set contains 350 image pairs sized 480×640 , captured by a DJI Phantom 3 Pro platform in Yardley, Pennsylvania, USA in 2017. We divided it into 300 training and 50 test samples. We did not label the train set, but for evaluation purposes, we manually labeled the ground truth by picking 4 pairs of correspondences for each test sample. The evaluation metrics are the same for the synthetic data.

In order to reduce training time, we finetune the synthetic data neural networks to the real data train set. We first downsize the original images of both training and test sets to 142×142 and then center-crop a patch of size 128×128 to avoid border effects. This downsizing reduces the accuracy of the homography estimation. For example, some important features are only a few pixels wide and will be lost during the downsampling. We compare these deep networks that use the downsized images with the feature based approaches on both full resolution images and downsized images. The low resolution images provide a fairer comparison as it standardizes the input for both the deep learning and feature-based methods. However, using full resolution images is standard practice for feature-based methods, and highlights the benefit of more granular inputs.

Our unsupervised neural network can directly use the downsized images since it does not use ground truth labels. However, for the supervised neural network, we need to use the synthetic data generation procedure to create 300 synthetic data samples from the downsized image pairs. We then fine tune both models over 30,000 iterations for roughly 9 hours. We evaluate each approach on the test sets 30

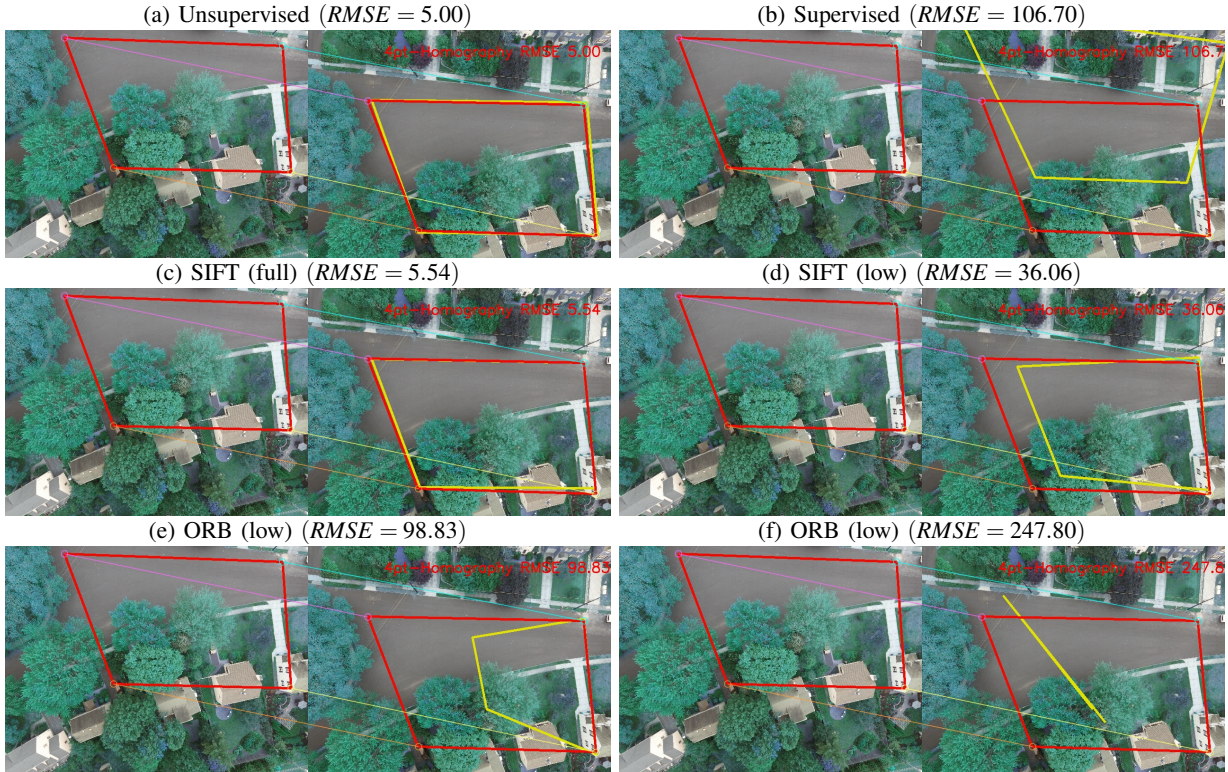


Fig. 7: Qualitative visualization of each estimation method. Unsupervised network and SIFT (full) have similar results. Supervised network fails and outputs close to identity homography. ORB (full) has worse performance than SIFT because it does not identify as many features. Both low resolution versions of SIFT and ORB cannot find good features and fail.

Approaches	N = 1	N = 20	N = 50
Unsupervised (GPU)	171.1	283.8	265.8
Unsupervised (CPU)	21.4	49.6	52.7
SIFT RANSAC (full)	1.4	1.7	1.7
SIFT RANSAC (low)	17.2	17.7	16.7
ORB RANSAC (full)	21.5	22.2	22.5
ORB RANSAC (low)	62.5	61.4	60.6

TABLE I: Frame Per Second (N is the mini-batch size). All the feature-based methods are run on the CPU. The neural network method on GPU has the highest throughput.

times and depict the average of 4pt-Homography RMSE and success rate in Fig. 5 and Fig. 6.

Our unsupervised method far outperforms the supervised method on the real data. In addition to having better baseline performance on the synthetic data set, our model is more adaptive and can take advantage of the real training images, while the supervised method still needs to synthetically generate data. This widening performance gap highlights the practical benefits of our unsupervised method not requiring ground truth labels.

Similar to our synthetic data results, our approach has a comparable performance with the full resolution SIFT, and is better than the full resolution ORB. In addition, it greatly outperforms all low-resolution feature-based approaches, including SIFT. The resolution decrease drops SIFT’s performance from 4.0 error to 49.0 error.

In terms of success rate, only the full-resolution SIFT can match the 100% success rate of our unsupervised approach. All the other methods have a relatively low success rate. For example, ORB with full resolution is 80% and ORB with low resolution is 72%. Fig. 7 is a qualitative view of the various methods that illustrates the above observations.

D. Running time

Another important criteria for practical application of homography estimation is the running time. We measure the inference time in frames per second (FPS) for all the methods. We omit the supervised network since it has an almost identical inference time to the unsupervised network. The feature-based methods are tested on a 16-core Intel Xeon CPU, and the deep learning methods are tested on the same CPU and an NVIDIA Titan X GPU.

As can be seen in Table I, our approach on the CPU has a running time close to ORB (low), and is much faster than SIFT (both full and low) and ORB (full). In addition, the parallel nature of our deep learning approach allows it to reach 265.8 fps on the GPU compared to 1.4 fps for SIFT(full). This efficient speed-to-performance tradeoff relative to the traditional approaches makes our approach especially useful in certain robotic applications that can exploit the parallel processing, such as image stitching.

VI. CONCLUSIONS

We have introduced an unsupervised algorithm that trains a deep neural network to estimate planar homographies. Our approach outperforms the corresponding supervised network on both the synthetic and real-world data sets, demonstrating the superiority of unsupervised learning in image warping problems.

Our approach additionally outperforms state-of-the-art feature-based methods in accuracy, robustness, and speed. The speed and adaptive nature of our algorithm makes it especially useful in robotics applications that can exploit parallel computation.

Finally, our approach is easily scalable to more general warping motions. Our findings provide additional evidence for applying deep learning methods, specifically unsupervised learning, to various robotic perception problems such as stereo depth estimation, or visual odometry. Our insights on estimating homographies with unsupervised deep neural network approaches provide an initial step in a structured progression of applying these methods to larger problems.

VII. ACKNOWLEDGEMENTS

We gratefully acknowledge the support of ARL grants W911NF-08-2-0004 and W911NF-10-2-0016, ARO grant W911NF-13-1-0350, N00014-14-1-0510, N00014-09-1-1051, N00014-11-1-0725, N00014-15-1-2115 and N00014-09-1-103, DARPA grants HR001151626/HR0011516850 USDA grant 2015-67021-23857 NSF grants IIS-1138847, IIS-1426840 CNS-1446592 CNS-1521617 and IIS-1328805, Qualcomm Research, United Technologies, and TerraSwarm, one of six centers of STARnet, a Semiconductor Research Corporation program sponsored by MARCO and DARPA. We would also like to thank Aerial Applications for the UAV data set.

REFERENCES

- [1] M. Brown, D. G. Lowe, *et al.*, "Recognising panoramas." in *ICCV*, vol. 3, 2003, p. 1218.
- [2] M. Shridhar and K.-Y. Neo, "Monocular slam for real-time applications on mobile platforms," 2015.
- [3] Z. Zhang and A. R. Hanson, "3d reconstruction based on homography mapping," *Proc. ARPA96*, pp. 1007–1012, 1996.
- [4] Z. Pan, X. Fang, J. Shi, and D. Xu, "Easy tour: a new image-based virtual tour system," in *Proceedings of the 2004 ACM SIGGRAPH international conference on Virtual Reality continuum and its applications in industry*. ACM, 2004, pp. 467–471.
- [5] C.-Y. Tang, Y.-L. Wu, P.-C. Hu, H.-C. Lin, and W.-C. Chen, "Self-calibration for metric 3d reconstruction using homography." in *MVA*, 2007, pp. 86–89.
- [6] D. Capel, "Image mosaicing," in *Image Mosaicing and Super-resolution*. Springer, 2004, pp. 47–79.
- [7] R. Szeliski, "Image alignment and stitching: A tutorial," *Foundations and Trends® in Computer Graphics and Vision*, vol. 2, no. 1, pp. 1–104, 2006.
- [8] B. D. Lucas and T. Kanade, "An iterative image registration technique with an application to stereo vision," in *Proceedings of the 7th International Joint Conference on Artificial Intelligence - Volume 2*, ser. IJCAI'81. San Francisco, CA, USA: Morgan Kaufmann Publishers Inc., 1981, pp. 674–679. [Online]. Available: <http://dl.acm.org/citation.cfm?id=1623264.1623280>
- [9] S. Baker and I. Matthews, "Lucas-kanade 20 years on: A unifying framework," *International journal of computer vision*, vol. 56, no. 3, pp. 221–255, 2004.

- [10] D. G. Lowe, "Distinctive image features from scale-invariant keypoints," *International journal of computer vision*, vol. 60, no. 2, pp. 91–110, 2004.
- [11] M. A. Fischler and R. C. Bolles, "Random sample consensus: A paradigm for model fitting with applications to image analysis and automated cartography," *Commun. ACM*, vol. 24, no. 6, pp. 381–395, June 1981. [Online]. Available: <http://doi.acm.org/10.1145/358669.358692>
- [12] F.-I. Wu and X.-y. Fang, "An improved ransac homography algorithm for feature based image mosaic," in *Proceedings of the 7th WSEAS International Conference on Signal Processing, Computational Geometry & Artificial Vision*. World Scientific and Engineering Academy and Society (WSEAS), 2007, pp. 202–207.
- [13] E. Rublee, V. Rabaud, K. Konolige, and G. Bradski, "Orb: An efficient alternative to sift or surf," in *Computer Vision (ICCV), 2011 IEEE international conference on*. IEEE, 2011, pp. 2564–2571.
- [14] P. Weinzaepfel, J. Revaud, Z. Harchaoui, and C. Schmid, "Deepflow: Large displacement optical flow with deep matching," in *Proceedings of the IEEE International Conference on Computer Vision*, 2013, pp. 1385–1392.
- [15] E. Ilg, N. Mayer, T. Saikia, M. Keuper, A. Dosovitskiy, and T. Brox, "FlowNet 2.0: Evolution of optical flow estimation with deep networks," *arXiv preprint arXiv:1612.01925*, 2016.
- [16] P. Fischer, A. Dosovitskiy, E. Ilg, P. Häusser, C. Hazırbaş, V. Golkov, P. van der Smagt, D. Cremers, and T. Brox, "FlowNet: Learning optical flow with convolutional networks," *arXiv preprint arXiv:1504.06852*, 2015.
- [17] J. Revaud, P. Weinzaepfel, Z. Harchaoui, and C. Schmid, "Deepmatching: Hierarchical deformable dense matching," *International Journal of Computer Vision*, vol. 120, no. 3, pp. 300–323, 2016.
- [18] H. Altwaijry, A. Veit, S. J. Belongie, and C. Tech, "Learning to detect and match keypoints with deep architectures." in *BMVC*, 2016.
- [19] D. Eigen, C. Puhrsch, and R. Fergus, "Depth map prediction from a single image using a multi-scale deep network," in *Advances in neural information processing systems*, 2014, pp. 2366–2374.
- [20] D. DeTone, T. Malisiewicz, and A. Rabinovich, "Deep image homography estimation," *arXiv preprint arXiv:1606.03798*, 2016.
- [21] T. Zhou, M. Brown, N. Snavely, and D. G. Lowe, "Unsupervised learning of depth and ego-motion from video," *arXiv preprint arXiv:1704.07813*, 2017.
- [22] M. Muja and D. G. Lowe, "Fast approximate nearest neighbors with automatic algorithm configuration." *VISAPP (1)*, vol. 2, no. 331-340, p. 2, 2009.
- [23] R. I. Hartley and A. Zisserman, *Multiple View Geometry in Computer Vision*, 2nd ed. Cambridge University Press, ISBN: 0521540518, 2004.
- [24] S. Baker, A. Datta, and T. Kanade, "Parameterizing homographies," *Technical Report CMU-RI-TR-06-11*, 2006.
- [25] K. Simonyan and A. Zisserman, "Very deep convolutional networks for large-scale image recognition," *arXiv preprint arXiv:1409.1556*, 2014.
- [26] F. N. Iandola, S. Han, M. W. Moskewicz, K. Ashraf, W. J. Dally, and K. Keutzer, "Squeezenet: Alexnet-level accuracy with 50x fewer parameters and 0.5 mb model size," *arXiv preprint arXiv:1602.07360*, 2016.
- [27] E. Dubrofsky, "Homography estimation," *Diplomová práce. Vancouver: Univerzita Britské Kolumbie*, 2009.
- [28] G. H. Golub and C. Reinsch, "Singular value decomposition and least squares solutions," *Numerische mathematik*, vol. 14, no. 5, pp. 403–420, 1970.
- [29] T. Papadopoulos and M. I. Lourakis, "Estimating the jacobian of the singular value decomposition: Theory and applications," in *European Conference on Computer Vision*. Springer, 2000, pp. 554–570.
- [30] R. Hartley and A. Zisserman, *Multiple view geometry in computer vision*. Cambridge university press, 2003.
- [31] M. Jaderberg, K. Simonyan, A. Zisserman, *et al.*, "Spatial transformer networks," in *Advances in Neural Information Processing Systems*, 2015, pp. 2017–2025.
- [32] M. Abadi, A. Agarwal, P. Barham, E. Brevdo, Z. Chen, C. Citro, G. S. Corrado, A. Davis, J. Dean, M. Devin, *et al.*, "Tensorflow: Large-scale machine learning on heterogeneous distributed systems," *arXiv preprint arXiv:1603.04467*, 2016.
- [33] D. Kingma and J. Ba, "Adam: A method for stochastic optimization," *arXiv preprint arXiv:1412.6980*, 2014.